ADVANCED MATERIALS
www.advmat.de

On-Demand Programming of Liquid Metal-Composite Microstructures through Direct Ink Write 3D Printing

Aaron Haake, Ravi Tutika, Gwyneth M. Schloer, Michael D. Bartlett, and Eric J. Markvicka**

Soft, elastically deformable composites with liquid metal (LM) droplets can enable new generations of soft electronics, robotics, and reconfigurable structures. However, techniques to control local composite microstructure, which ultimately governs material properties and performance, is lacking. Here a direct ink writing technique is developed to program the LM microstructure (i.e., shape, orientation, and connectivity) on demand throughout elastomer composites. In contrast to inks with rigid particles that have fixed shape and size, it is shown that emulsion inks with LM fillers enable in situ control of microstructure. This enables filaments, films, and 3D structures with unique LM microstructures that are generated on demand and locked in during printing. This includes smooth and discrete transitions from spherical to needle-like droplets, curvilinear microstructures, geometrically complex embedded inclusion patterns, and connected LM networks. The printed materials are soft (modulus < 200 kPa), highly deformable (>600 % strain), and can be made locally insulating or electrically conductive using a single ink by controlling the process conditions. These capabilities are demonstrated by embedding elongated LM droplets in a soft heat sink, which rapidly dissipates heat from high-power LEDs. These programmable microstructures can enable new composite paradigms for emerging technologies that demand mechanical compliance with multifunctional response.

1. Introduction

Additive manufacturing (AM) of soft materials has enabled the rapid design and fabrication of a wide range of materials and complex geometries.[1–6] These advancements in manufacturing have led to an emergence of soft matter devices that have tunable physical and functional properties across various length scales, creating soft multifunctional materials including active shape morphing,[7–10] soft pneumatic channels to create robots,[11–13] and electrically conductive materials.[14–20] To push these devices toward all soft matter systems, an emerging architecture is to create solid–liquid composite materials with liquid-phase fillers dispersed in soft elastomers. LMs like eutectic gallium–indium (EGaIn) have been of particular interest due to their low viscosity, low toxicity, high electrical and thermal conductivity, and rapid formation of a surface oxide.[21] This surface oxide forms nearly instantaneously at low oxygen concentration and allows for physical droplet manipulation and retention of metastable shapes.[22–25] LM-based solid–liquid composites, can be engineered to exhibit a wide range of material properties—including extreme toughening,[26] exceptional electrical and thermal properties;[27–34] shape-morphing;[35–37] stiffness tuning;[38,39] and the ability to form electrically conductive pathways through controlled mechanical pressure,[40–43] deformation,[44] and laser patterning.[45]

Key to these composites is the ability of the LM droplets to reconfigure their shape, orientation, and connections. In particular, control over LM microstructure ranging from spherical to ellipsoidal droplet shapes to connected droplet networks is essential for achieving advanced functions and properties; including over 10× enhancements in electrical conductivity, material toughness, and thermal conductivity.[26,44,46] For example, by reconfiguring isolated spherical LM droplets into a connected network, an initially insulating film can be transformed into electrically conductive traces, which are also self-healing by the subsequent reconfiguration of droplets from damage events.[40,47,48] Strain-invariant electrical resistance,[25,40,44,49,50] which goes against kinematic predictions from Pouillet's law, can be achieved as droplet networks deform under strain. While isolated ellipsoidal and oriented LM droplets create thermally conductive pathways to increase thermal conductivity over spherical droplets and deflect cracks to increase toughness.[26,46,51] These previous works demonstrate

A. Haake, E. J. Markvicka
Department of Mechanical & Materials Engineering
Smart Materials & Robotics Lab
University of Nebraska–Lincoln
Lincoln, NE 68588, USA
E-mail: eric.markvicka@unl.edu

R. Tutika, G. M. Schloer, M. D. Bartlett
Department of Mechanical Engineering
Soft Materials and Structures Lab
Virginia Tech
Blacksburg, VA 24060, USA
E-mail: mbartlett@vt.edu

R. Tutika, M. D. Bartlett
Macromolecules Innovation Institute
Virginia Tech
Blacksburg, VA 24060, USA

E. J. Markvicka
Department of Electrical & Computer Engineering
University of Nebraska–Lincoln
Lincoln, NE 68588, USA

The ORCID identification number(s) for the author(s) of this article can be found under https://doi.org/10.1002/adma.202200182.

DOI: 10.1002/adma.202200182

that material properties and performance are strongly dependent upon droplet microstructure and connectivity, spatial placement and orientation, and volume loading. However, common fabrication approaches using bulk replica molding, soft lithography, or patterning techniques result in primarily spherical inclusions with little control of shape, orientation, or spatial placement.[52,53] Meanwhile, connected LM droplet networks are typically formed using secondary operations or through the addition of a rigid filler. New fabrication processes are needed to enable spatial control of inclusion morphology and connectivity during fabrication to achieve programmable LM microstructures for systematic control of material properties and device performance.

Direct ink writing (DIW) is a filament-based AM method that allows printing of high-viscosity fluids, concentrated polymer solutions, and high-volume percent fillers at ambient conditions.[1] A variety of DIW methods and inks have been developed to achieve alignment of fillers such as magnetic particles,[7,54] liquid crystal molecules,[8,55,56] high-aspect ratio fibers,[57–59] and cellulose fibrils.[10] While the orientation of fillers can be controlled, the aspect ratio remains fixed during printing due to the relatively rigid, non-deformable properties of the filler. Recently, the ability to DIW emulsions with LM inclusions was demonstrated, however the combination of printing process conditions and LM droplet size resulted in primarily spherical inclusions.[31,60–63] Liquid inclusions can be elongated under mechanical deformation by inducing unrecoverable plastic strain[46] or thermal annealing of composites after stretching,[51] however these approaches require specific materials, lack spatial control, and only allow for elongation of inclusions along a single axis. Stand alone gallium-based LMs can also be patterned using DIW methods to create continuous LM structures and electrical circuits.[64–71] These structures are electrically conductive due to the continuous nature of the LM structures and are often combined and encapsulated with secondary inks such as elastomeric materials to provide electrical insulation and stability. The additional encapsulation steps are often required to prevent flow of the LM, electrically insulate the structures, and prevent interactions with other metals, which can cause alloying, corrosion, or embrittlement.[72] While significant progress has been made toward achieving spatial control of composition, structure, and properties during DIW, emulsion-based inks offer new opportunities to not only control orientation but the shape and connectivity of LM fillers during the fabrication process.

Here, we introduce a new DIW 3D printing strategy to achieve on-demand programming of LM-composite microstructures throughout a printed part. The functional emulsion ink consists of spherical LM microdroplets dispersed in a prepolymer matrix that can be printed and then cured into a soft and highly extensible elastomeric composite. By systematically controlling the printing process conditions and LM droplet size, we were able to transform the initially spherical LM droplets into highly elongated and orientated ellipsoids on demand at any location with very high aspect ratios (AR; major/minor ellipsoid axis). The rapid formation of the surface oxide locks these droplets into the programmed shape and allows for systematic control of the LM droplet microstructure throughout a printed part. In addition to shape and orientation, we can also transform the initially isolated LM droplets into a connected network, enabling local creation of insulating or electrically conductive regions using a single ink and manufacturing system by controlling the process conditions. This on-demand spatial control of LM microstructure (i.e., shape, orientation, and connectivity) has not been demonstrated with currently available casting, stretching, or patterning approaches. To rationally guide the DIW printing process, we created a quantitative design map as a function of the printing parameters, which shows that the LM microdroplet AR increases with nondimensionalized nozzle velocity and decreasing nozzle height. Utilizing the quantitative design map, we printed elastomer composites with unique LM microdroplet patterns such as smooth and discrete transitions from spherical to needle-like microstructures, curvilinear microstructures, geometrically complex thermal patterns, and embedded heat spreaders. We also create 3D structures that contain spatial variations in droplet shape in 3D configurations. These capabilities not only advance the manufacturing of LM-composites, but demonstrate new capabilities in DIW to tune inclusion shape, orientation, and connectivity on demand in composite materials, which is achieved through the use of liquid-phase fillers and is uniquely enabled by LM inclusions rapidly forming a surface oxide shell to lock in the programmed microstructure. The systematic integration of DIW 3D printing with advanced multifunctional materials provides opportunities to create composite architectures for emerging technologies such as soft robotics, human-machine interaction, and wearable electronics that demand mechanical compliance with a highly tunable functional response.

2. Results and Discussion

2.1. Direct Ink Write 3D Printing of Functional Emulsion Inks

For DIW of functional emulsion inks, the ink is loaded into a syringe and the material is extruded from the nozzle at a desired flow rate using a mechanically driven syringe pump, while the nozzle is moved laterally along a substrate (**Figure 1**a). The functional emulsion ink consists of LM microdroplets dispersed in a silicone prepolymer, which has been previously demonstrated.[27,33] The emulsion ink is fabricated with three different LM microdroplet diameters (D = 20, 100, and 200 μm; see Section 4 for more details). We can spatially control the orientation and AR of the LM microdroplets in the extruded filament by controlling printing parameters including: i) the nondimensionalized nozzle velocity ($V^* = V/C$), which represents the ratio of the nozzle velocity (V) to extrusion velocity (C), and ii) the nozzle height (H) along a straight motion path. Systematically controlling the printing parameters V^* and H results in a gradual and controlled change in the AR of the LM microdroplets with high-AR fillers aligning along the printing direction (Figure 1b). The left side of the filament in Figure 1b, printed at low $V^* = 1$ and high H = 300 μm, contains mostly spherical droplets (AR ≈ 1). As the printing progresses toward the right side, where the nozzle velocity is increased ($V^* = 15$) and the nozzle height is decreased (H = 20 μm) simultaneously, there is a transition from spherical to highly elongated microstructures with AR > 35. An optical microscopy image of the

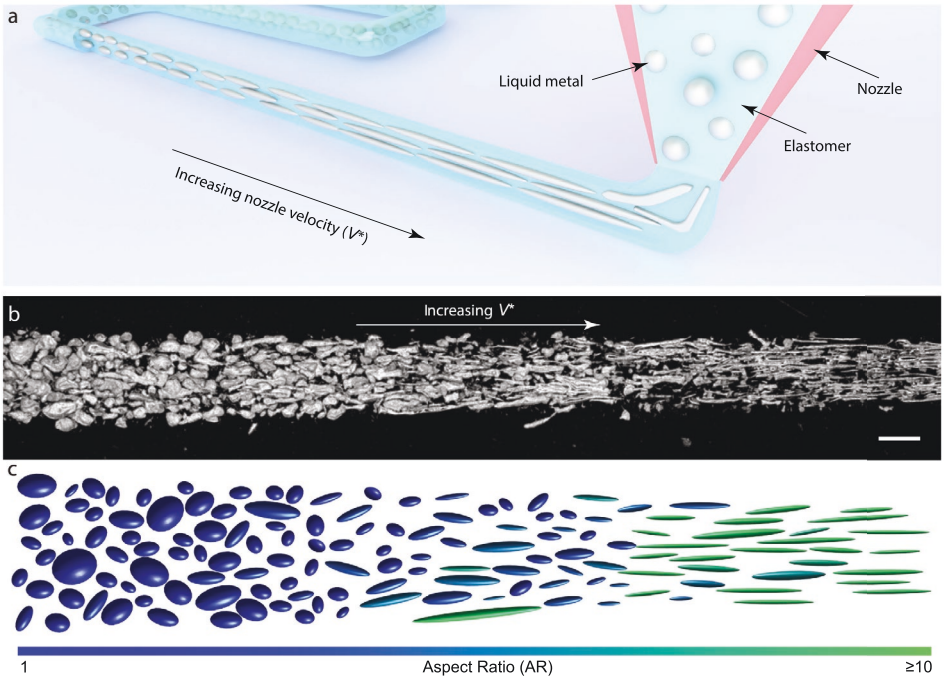

Figure 1. Directly programming LM microstructure through printing. a) Schematic representation of the printing setup showing the capability to alter LM microdroplet AR in situ. b) Photograph to illustrate the process control that can cause a gradual change in AR by simultaneously changing the printing velocity and height, scale bar = 500 µm. c) Image-analysis-based visualization of the printed filament LM microstructure showing an increase in average AR from AR = 1.4 to 10.5 with the highest AR > 35 as V^* is increased from 1 to 15 and H is decreased from 300 to 20 µm.

extruded filament was analyzed and ellipses were fit to the LM droplets. This data was used to create a visualization of the printed filament microstructure in MATLAB which highlights the evolution and control of droplet morphology as shown in Figure 1c. This demonstrates that a single AM system and functional emulsion ink can print filaments with a wide range of LM microstructures, ranging from spherical droplets (AR = 1) to high-AR, needle-like microstructures (AR > 35) where the embedded spherical LM droplets are physically transformed at the printing nozzle and locked-in by the rapid formation of the oxide shell.

2.2. On-Demand Programming of LM Microstructure

A cross section of the printing nozzle is illustrated in **Figure 2**a and indicates the relevant parameters in the printing process. Printed filaments were characterized using optical microscopy, and droplet analysis was performed to measure the droplet AR. Figure 2b shows representative results using a 3D visualization from the microstructural analysis. Here, the printed filament microstructure represents a combination of $V^* = 1$, and $H = 20$ µm, which yields mostly spherical droplets with AR ≤ 5. As the nozzle velocity is increased to $V^* = 12$ and the printing height is maintained at $H = 20$ µm, droplet AR ≥ 10 are observed with maximum AR approaching 40, as shown in the 3D visualization of the LM microstructures (Figure 2c,g). These printed filaments with programmed microstructure represent the extremes of the evaluated process space and demonstrate the enabling role of our DIW process with functional emulsion inks to achieve on-demand control of LM microstructure.

To systematically study the influence of printing parameters on the programmed LM microstructure, we independently investigated three parameters: i) the diameter (D) of the LM microdroplets in the emulsion ink, ii) the nondimensionalized nozzle velocity (V^*), and iii) the height of the nozzle from the printing bed (H). The influence of LM microdroplet diameter on LM microstructure for a given printing velocity and nozzle height ($V^* = 12$, and $H = 20$ µm) is shown in Figure 2d. We observed that the AR of the LM microdroplets increases with increasing diameter, with emulsion inks containing $D = 200$ µm droplets showing the highest AR after printing. The emulsion inks containing $D = 20$ µm droplets show relatively little change in AR, which is attributed to the increase in stiffness of smaller droplets due to surface oxide and surface tension, which increases the droplets' resistance to deformation.[52] The AR of droplets could also be increased by increasing V^* from 1 to 12 while maintaining the same printing height and droplet size ($H = 20$ µm and $D = 200$ µm). Figure 2e shows the V^*-dependent microscopy images, where the mean AR increases from 1.6 to 7.9 as V^* increases from 1 to 12. However, with the same printing velocity and droplet size ($V^* = 12$ and $D = 200$ µm), AR decreases as the printing height is increased from 20 to 250 µm. The filaments also tend to break into sections at the highest printing height with droplet AR close to 1, as shown in Figure 2f.

To guide the programming of LM microstructures and the selection of printing parameters for the new DIW strategy, we examined AR as a function of printing conditions. We

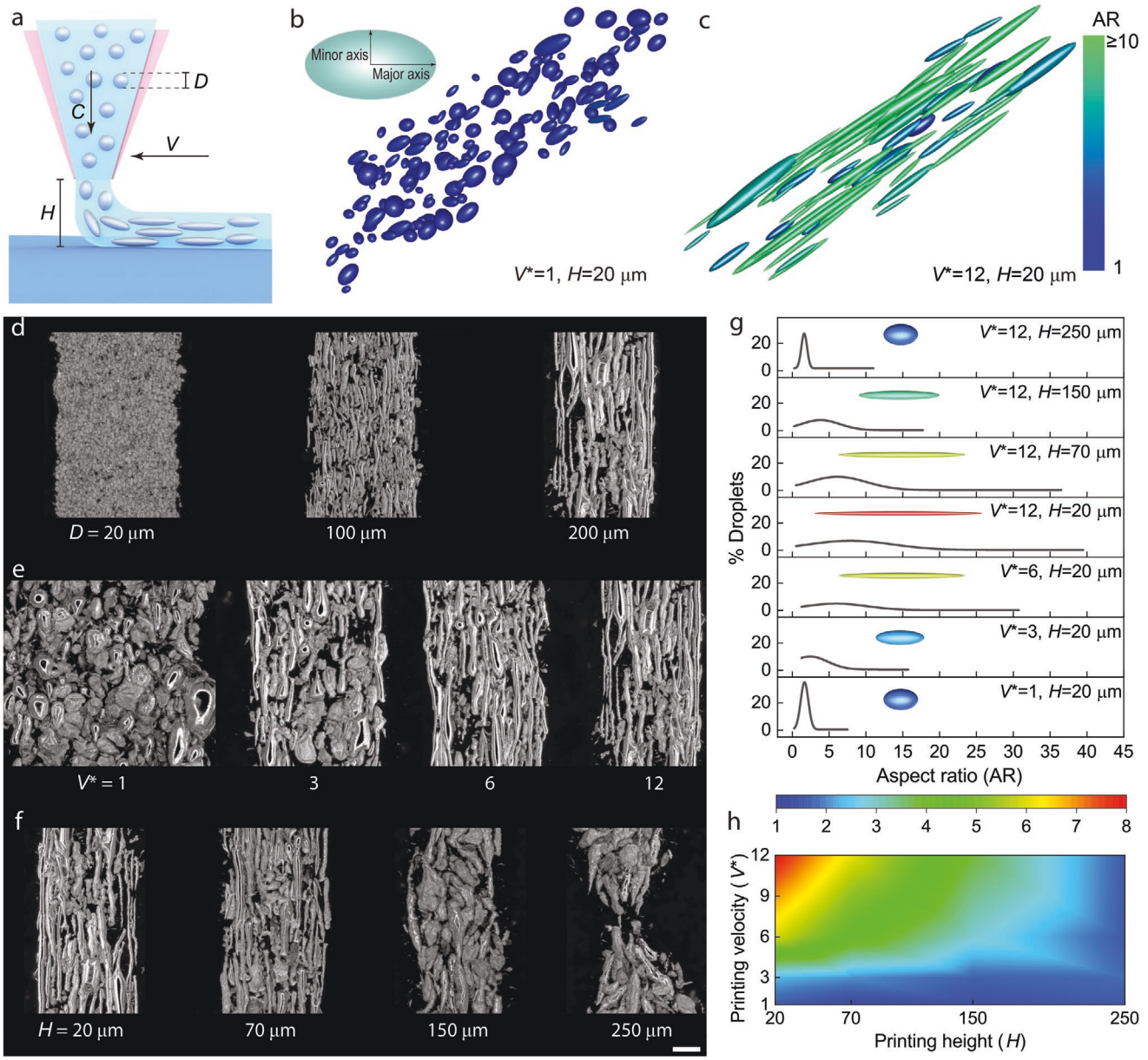

Figure 2. Printing LM emulsion inks with direct ink writing. a) Schematic representation of the printing nozzle cross section. b,c) 3D visualization of the LM droplets for printing parameters H = 20 μm and V^* = 1 (b) and H = 20 μm and V^* = 12 (c) (image analysis assumes minor axes $b = c$ for all ellipsoids). d–f) Optical microscopy images of printed filaments for printing condition V^* = 12, H = 20 μm, and D = 20, 100, 200 μm (d), V^* = 1, 3, 6, 12, H = 20 μm, and D = 200 μm (e), and V^* = 12, H = 20, 70, 150, 250 μm, and D = 200 μm (f). Scale bar = 200 μm for (d–f). g) Gaussian fits to the droplet analysis histograms of the microscopy images in (e) and (f) showing the droplets as a function of AR for each condition. The inset droplets represent the mean AR for the corresponding condition and the color is from the color map in (h). h) Color map of mean AR as a function of printing velocity (V^*) and height (H) obtained from (g).

performed particle analysis for the filaments printed with D = 200 μm droplets, shown in Figure 2d–f, and applied a Gaussian fit to the AR histograms. Figure 2g shows the resulting Gaussian fits where the droplet inset shows the mean AR and the lowest and highest AR droplets are shown as the terminal x-axis values of the Gaussian fit. The highest AR resulted from the highest V^* and lowest H condition (V^* = 12, and H = 20 μm) with the AR of some droplets approaching 40. A design map was then created from 16 independent experiments, where the mean AR from the Gaussian fits were plotted as a color map as a function of the printing parameters with V^* on the y-axis and H on the x-axis (Figure 2h). The optical microscopy images and Gaussian fits from the independent experiments are shown in Figures S1 and S2, Supporting Information, respectively. The color map shows how increasing nozzle velocity (V^*) and decreasing nozzle height results in a higher mean AR. The same AR trend is observed when looking at the maximum AR achieved as a function of V^* and H, as shown in the design map in the Supporting Information (Figure S3, Supporting Information). These quantitative design

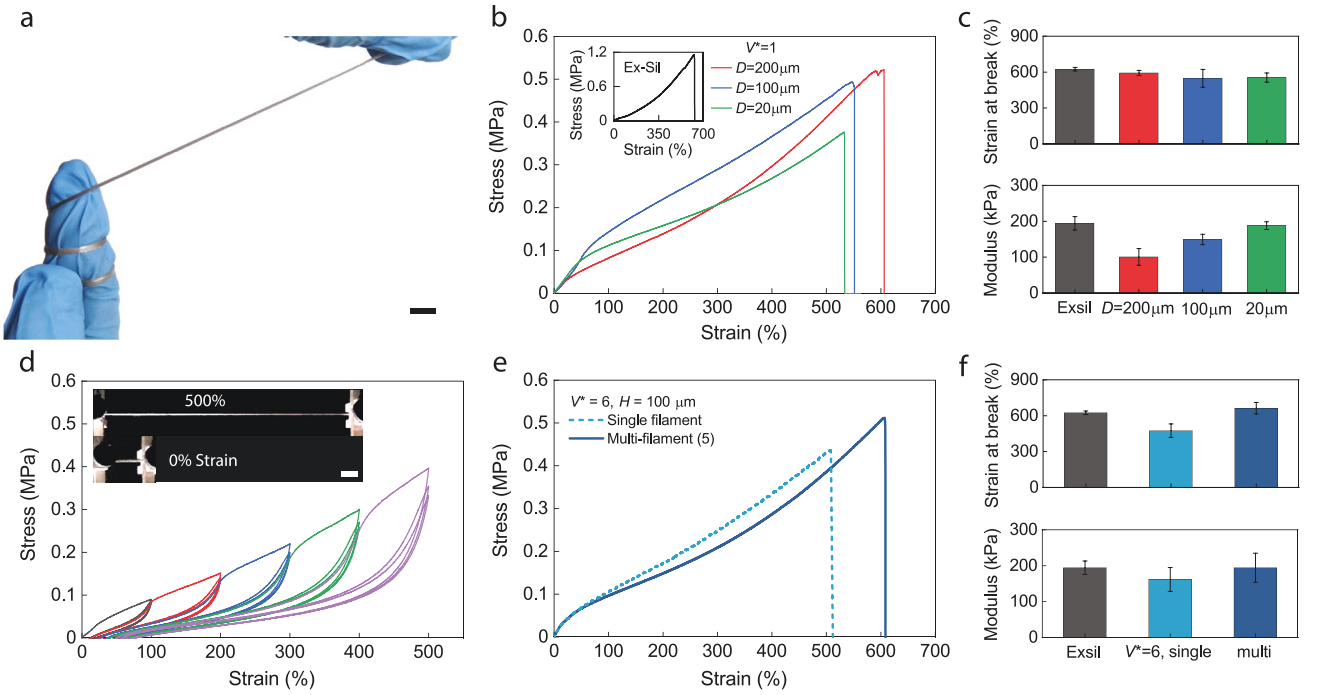

Figure 3. Mechanical properties of printed composites. a) Photograph showing the stretchable and soft mechanics of a filament stretched 4× its original length. Scale bar = 5 mm. b) Stress–strain curves of pure elastomer (Ex-Sil) and composite filaments with different droplet sizes stretched in tension for $V^* = 1$, $H = 100$ μm, and $D = 20$, 100, 200 μm. c) Strain at break and tensile modulus calculated from stress–strain curves. $n = 3$, data presented as mean ± SD. d) Cyclic test of a composite filament ($V^* = 1$, $H = 100$ μm, and $D = 200$ μm) with three cycles at every 100% strain increment up to 500% strain. The colors indicate the three cycles at each strain increment. Inset shows photograph of a filament at 0% and 500% strain stretched in tension. Scale bar = 20 mm. e) Stress–strain curves for a single and multifilament composites stretched in tension for $V^* = 6$, $H = 100$ μm, and $D = 200$ μm. f) Strain at break and tensile modulus calculated from the stress–strain curves. $n = 3$, data presented as mean ± SD.

maps provide a tool to create LM-composite microstructures from generally spherical droplets to highly elongated droplets by varying the printing conditions. This allows for systematic control of material microstructure where the shape and orientation of LM inclusions can be readily tuned during composite fabrication. Although high-AR solid particles can be aligned during DIW, the design map in Figure 2h shows that the AR of LM droplets can be systematically tuned on demand with alignment occurring along the printing path without modifying the base ink. Therefore, this LM emulsion printing technique controls multiple aspects of composite microstructure in a single fabrication process.

2.3. Mechanical Properties of Printed Filaments and Films

The DIW of LM-composites results in materials that are soft and highly deformable due to the combination of a soft elastomer with liquid-phase inclusions. This is demonstrated in **Figure 3**a where the printed filaments can be stretched and easily wrapped around a human finger. To quantify their mechanical properties, the filaments were stretched in uniaxial tension until they failed and the stress–strain curves were analyzed. Figure 3b shows the deformation behavior for filaments with $V^* = 1$, $H = 100$ μm, and $D = 20$, 100, and 200 μm with the stress–strain curve for pristine silicone elastomer in the inset. Tensile modulus (up to 5% strain) and strain at break were calculated for each sample filament and the mean and standard deviation for three filaments are plotted in Figure 3c. The strain at break data indicates that the printed composite filaments and silicone elastomer filaments are both highly stretchable, with failure strains of ≈600% for all conditions. However, the tensile modulus data shows a softer response for filaments with larger LM droplets with an increasing modulus as droplet size decreases.

The printed composite filaments can also be stretched over multiple loading cycles. This was evaluated by stretching a filament printed with $V^* = 1$, $H = 100$ μm, and $D = 200$ μm up to 500% strain in 100% increments with three cycles at each increment (Figure 3d). We see a characteristic soft composite cyclic response, where the first cycle to a given strain shows hysteresis, while subsequent loading cycles show little hysteresis. This is commonly referred to as the Mullen's effect, and is observed in many soft composites, including LM-composites that are fabricated through casting.

The printing process can produce single filaments as well as multifilament geometries. We evaluate the mechanical response of single and multifilament samples with printing condition $V^* = 6$, $H = 100$ μm, and $D = 200$ μm in uniaxial tension and plotted the stress–strain curves in Figure 3e. Figure 3f shows that both the single and multifilament samples with elongated LM droplets show comparable strain at break and modulus behavior to the pristine silicone elastomer. We found that the single filament geometry shows a reduced strain at break and modulus relative to the multifilament sample. We attribute this to minor inconsistencies in the cross-sectional

area that likely play a more significant role in the mechanical response of single filaments relative to multifilament geometries. In both geometries, the material was still highly extensible (strain at break ≈ 600%) and soft (modulus ≈ 200 kPa), showing the ability to print soft and deformable composites with highly elongated LM inclusions.

2.4. Programmable LM Microstructures in 2D and 3D

The DIW strategy for controlling LM microstructure throughout a printed part enables us to create single layer films and multilayer structures with varying inclusion morphology using a single ink and AM system. By following a curve instead of a straight motion path, we could create nonlinear, high-AR LM microstructures with shapes that mimic the print path. Here, we demonstrated this ability by printing a spiral pattern. The optical microscopy image of the printed film is shown in **Figure 4**a. A section of the printed film is highlighted and a schematic illustration and optical microscopy image is shown in Figure 4b,c, respectively. In addition to creating printed parts with homogeneous microstructure, the printing conditions (V^*, H) can be actively tailored throughout the printing process to achieve spatial control of the LM microstructure (Figure S4a,

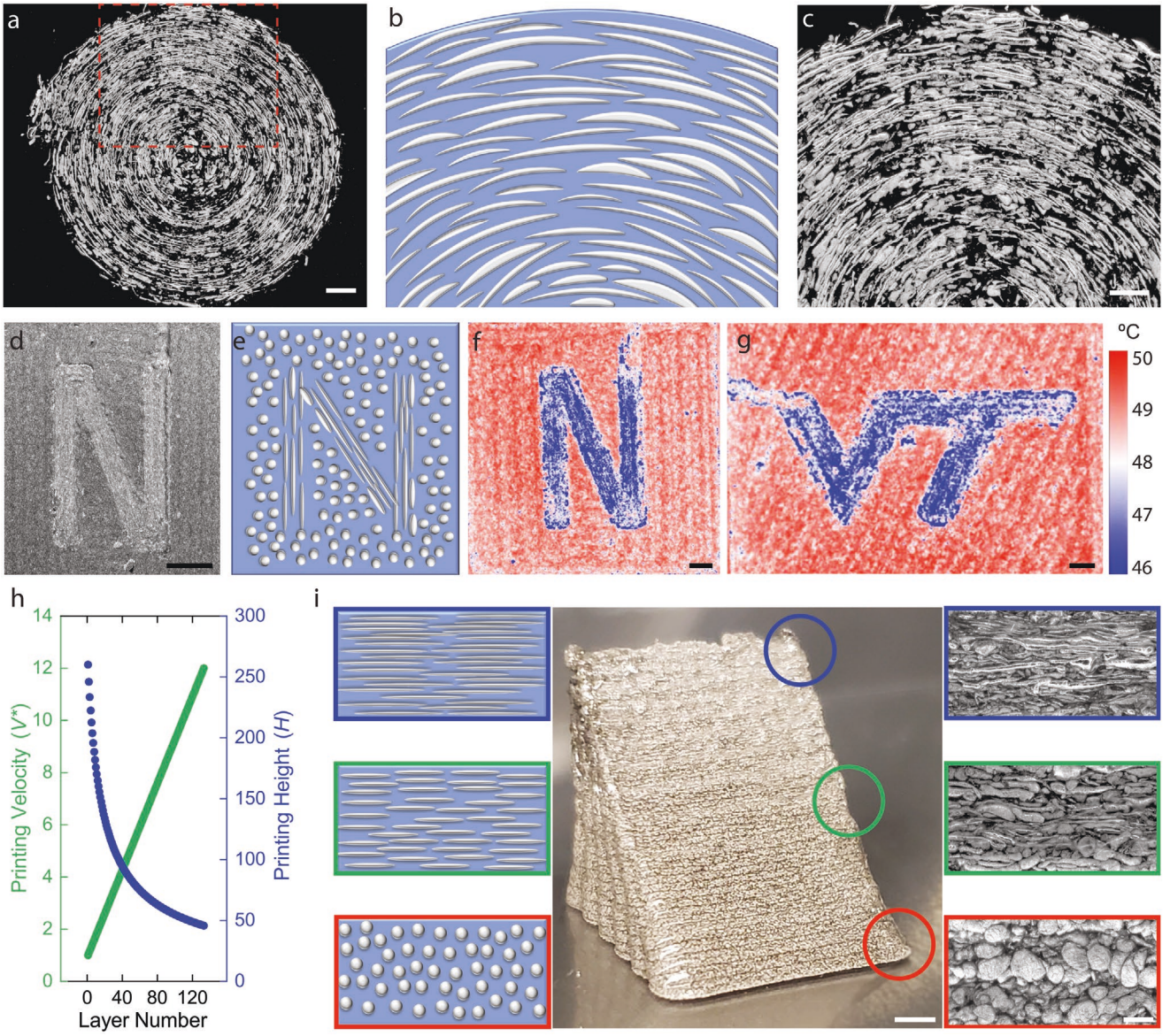

Figure 4. Direct ink writing of printed parts with programmable LM microstructure. a) Optical micrograph of a printed film with nonlinear, spiral motion path. Scale bar = 1 mm. b) Schematic illustration of the printed microstructure and c) optical microscopy image of the highlighted section shown in (a). Scale bar = 500 µm. d) Optical microscopy image (scale bar = 5 mm) and e) schematic illustration of a printed film with embedded thermal pattern of the letter "N". Infrared image of the f) "N" and g) "VT" thermal pattern when uniformly heated. Scale bar = 2 mm. h) Plot of printing velocity (V^*) and printing height (H) as a function of layer number for the 3D structure presented in (i). i) Photograph of a fully filled right angled triangular prism printed (133 layers) with schematic illustrations and optical microscopy images (scale bar = 200 µm) of LM droplet morphologies at top, middle, and bottom sections of the structure respectively. Scale bar = 2 mm for macro photograph in (i).

Supporting Information). Here, discrete transitions in microstructure were achieved by controlling the printing conditions to attain alternating paths of low AR (V^* = 2, H = 210 μm, D = 200 μm) and high-AR (V^* = 12, H = 70 μm, D = 200 μm) LM droplets. A section of the printed film is highlighted and a schematic illustration and optical microscopy image are shown in Figure S4b,c, Supporting Information, respectively. Smooth, continuous transitions from spherical to needle-like microstructures can also be achieved in a single filament (Figure 1b) or throughout a printed film.

To further demonstrate the ability to spatially control the LM microstructure, microstructural patterns can be embedded in the printed structure. This allows for the embedding of different functional properties throughout a part. We demonstrated spatial control of LM microstructure by printing the letter "N" with high AR (V^* = 12, H = 70 μm, and D = 200 μm) LM droplets, with spherical (V^* = 2, H = 210 μm, and D = 200 μm) LM droplets surrounding the letter. Figure 4e shows a schematic illustration of the programmed LM microstructure shown in Figure 4d. When the sample is uniformly heated, the difference in LM microstructure results in a difference in heat transfer characteristics and the letter "N" is visible when viewed with an infrared (IR) camera (Figure 4f). As expected, the letter "N" that is constructed with needle-like microstructures remains at a lower temperature than the surrounding matrix due to the higher thermal conductivity.[46,51] A similar IR image of a printed film that contains the printed letters "VT" with high-AR LM microstructures is presented in Figure 4g (IR thermal video for Figure 4f,g can be found in Movie S1, Supporting Information). An optical microscopy image of the printed film and schematic illustration of the LM microstructure can be found in the Supporting Information (Figure S5, Supporting Information).

Finally, we demonstrated the ability of our DIW strategy to program LM microstructure in multilayer and 3D structures. First, a ten-layer structure was created, where each layer is printed with high-AR LM droplets as illustrated in Figure S4d–f, Supporting Information. Similar LM microstructures were observed throughout the multilayer structure, as shown in the optical microscopy images of the first and final layer of the printed film (Figure S4f, Supporting Information). We expand upon this homogeneous multilayer structure and show that LM microstructure can also be varied throughout a 3D structure by controlling the printing parameters V^* and H for each individual layer (Figure 4h; see Section 4 for more details). Here we program a smooth transition from spherical (V^* = 2, H = 260 μm, and D = 200 μm) to high-AR (V^* = 12, H = 45 μm, and D = 200 μm) LM droplets to print a fully filled right angled triangular prism as shown in Figure 4i. This manufacturing strategy allows us to change the LM droplet microstructure throughout the printing process, as shown in the optical microscopy images (Figure 4i, right). The printed films and 3D structures emphasize the versatility of our new approach to spatially tailor the LM droplet microstructure throughout a 2D or 3D printed part. This allows us to achieve geometrically complex LM microstructures that can not be created through film casting, mechanical deformation, magnetic alignment, replica molding, or lithography.

2.5. Multilayer, Multimaterial DIW 3D Printing for Thermal Management

To further demonstrate the versatility of the DIW strategy to program LM-composite microstructures, we printed a multilayer, multimaterial soft heat sink. We utilized two extrusion-based print heads to create a 15-layer part with two regions of pure silicone elastomer (E1, E2) and two regions of the LM-composite containing oriented LM droplets (LM1, LM2) using the following printing parameters V^* = 12, H = 70 μm, and D = 200 μm. A schematic illustration of the programmed LM microstructure is shown in **Figure 5**a (left). A video of the multilayer, multimaterial printing process for layers one to three can be found in Movie S2, Supporting Information. After printing, we assembled an LED circuit on the part surface with high-power LEDs connected in series with LM interconnects (Figure 5a, right). The sample was placed on an aluminum block, and a current of 0.5 A was applied to the 4-LED circuit for 40 s and then switched off. The high-power LEDs generated a significant amount of heat while in operation, and the thermal signature of the LEDs was tracked through an IR camera. Figure 5b (blue curve) shows that the LEDs in the oriented-LM regions (LM1, LM2) only reached a maximum temperature of 40 °C with a nearly symmetric heating and cooling profile, which illustrates rapid and well-controlled heat transfer. The pure silicone elastomer regions (E1, E2) accumulated heat at and around the LEDs, which reached temperatures greater than 100 °C with a slower cooling profile as shown by the red curve in Figure 5b. A sequence of frames from the IR thermal imaging (Movie S3, Supporting Information) is presented in Figure 5c, which shows that the printed LM-composite regions with programmed LM microstructures remained much cooler throughout the experiment and performed passive thermal management efficiently. This demonstration illustrates the ability to effectively control thermal dissipation at different regions throughout a printed part utilizing the DIW 3D printing process to control material composition and LM-composite microstructure throughout a multilayer part.

2.6. LM-Composite Microstructure Control and Formation of Connected Networks

The DIW strategy for programming LM-composite microstructures enables the fabrication of 3D multilayered structures consisting of isolated LM droplets with controllable shape and orientation. These microstructures are important for applications that require electrical insulation. To enable applications where electrical conductivity is needed, the formation of LM networks is essential. Therefore, the ability to control LM microstructures from spherical to ellipsoidal to connected networks can open possibilities to print composites with diverse functionalities. Here, using the same emulsion ink and manufacturing system, we demonstrate that the initially isolated LM droplets could be printed and then reconfigured into a connected network of LM droplets to form electrically conductive traces. **Figure 6**a illustrates the different print processing conditions that are utilized to achieve full control of LM droplet shape, orientation, and connectivity throughout a printed part.

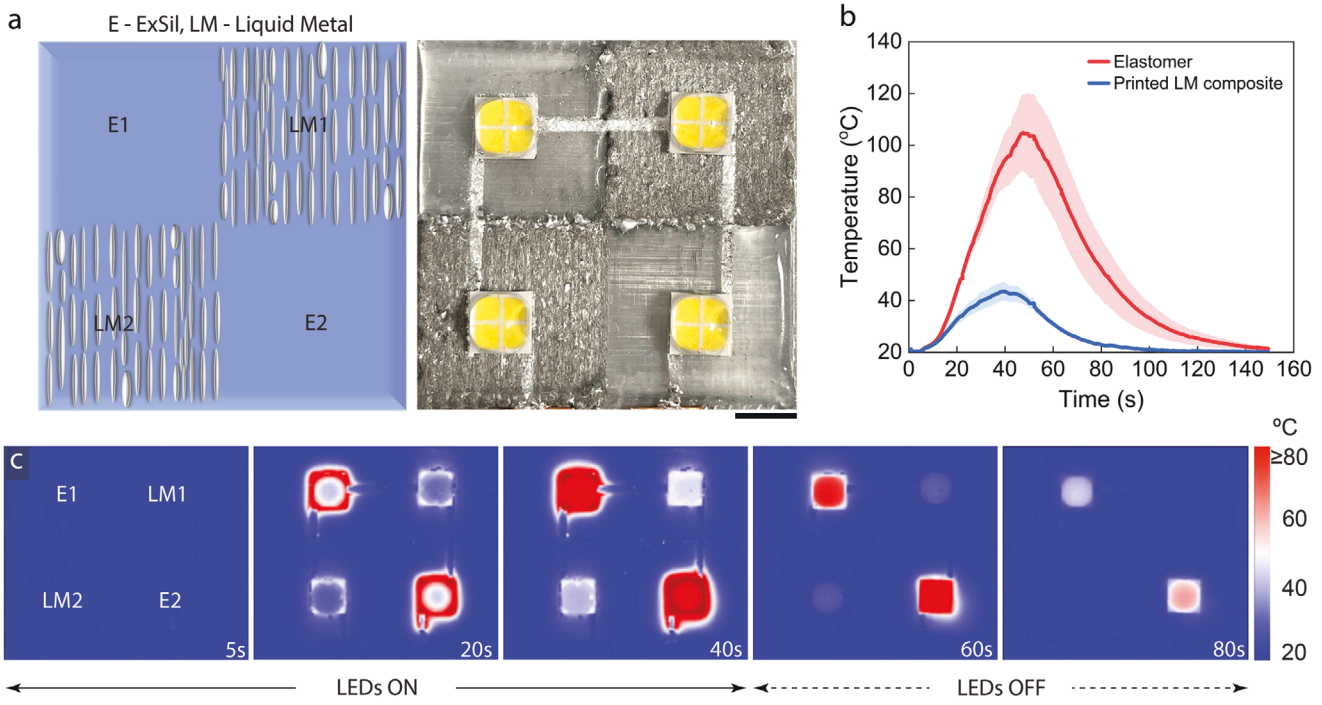

Figure 5. Heterogeneous, printed LM-composite heat sink. a) Top-view schematic and photograph of the multilayer, multimaterial printed heat sink (LM droplets oriented vertically) with highpower LEDs connected through mask-deposited LM interconnects on the top surface. Scale bar = 5 mm. b) Plot of average temperature of the LEDs in unfilled silicone elastomer and composite elastomer with oriented LM droplet regions, shaded regions represent the SD of the two regions. c) Thermal camera images illustrate the efficient and contrasting heat transfer characteristics of the composite regions LM1, LM2 that keep the LEDs cool.

Leveraging the quantitative design map, a single extrusion-based print head and emulsion ink was used to create a single layer film with graded particle morphology (Figure 6b). A schematic illustration of the printed film is shown in Figure 6c. The morphology gradient was created by varying the printing parameters from $V^* = 2$, $H = 217$ µm to $V^* = 12$, $H = 41$ µm using $D = 200$ µm LM droplets. The isolated droplet regions were electrically insulating at length scales greater than the droplet size (Figure S7, Supporting Information). The initially isolated LM droplets can be transformed into a connected network through a tapping motion with the printing nozzle (see Section 4 for more details). The formed LM networks were electrically conductive and can be used to create electrical circuits (Figure S8, Supporting Information). The ability to print diverse LM droplet morphologies and form conductive networks using a single ink and single print head enables the fabrication of complex microstructures in soft LM-composites. With this new DIW 3D printing strategy, both insulating and electrically conductive soft materials can be rapidly fabricated with programmable properties throughout a printed part.

3. Conclusion

We have demonstrated spatial control of LM droplet microstructure in elastomer composites through a DIW 3D printing process. The interplay between the printing velocity, printing height, and the LM droplet size in the DIW setup leads to controllable droplet architectures (i.e., shape, orientation, and connectivity). The liquid nature of the gallium–indium LM alloy with rapidly forming surface oxide in combination with the DIW process enables programmable architectures in a rapid single step process without the need for post processing. This allows for highly tunable microstructures throughout a manufactured part that can enable spatial programming of material properties. The nearly instantaneous formation of the LM oxide shell is key to this printing process as it allows for on-demand formation of non-spherical droplets that are rapidly locked into shape during printing. We hypothesize that the oxide shell prevents surface tension from restoring the droplet to a spherical shape. The rapid oxide formation coupled with the droplet elongation generated during printing enables the on-demand creation of unique microstructures in the printed filament, including smooth and discrete transitions from spherical to needle-like droplets with ARs as high as 40, curvilinear microstructures, connected LM networks, and geometrically complex embedded inclusion patterns. We demonstrate the spatial LM microstructure control by creating films and 3D structures with unique LM microstructure gradients and patterns. Although we demonstrated the functionality of the printing process by creating a passive heat spreader for an LED circuit, the new DIW 3D printing process could be utilized to print parts with programmable and anisotropic properties for actuators, sensors, and circuits for soft robotics and electronics. The combination of the solid–liquid composites with our new DIW fabrication approach provides capabilities and insights to the AM and LM communities to develop advanced materials and devices with exceptional multifunctional capabilities.

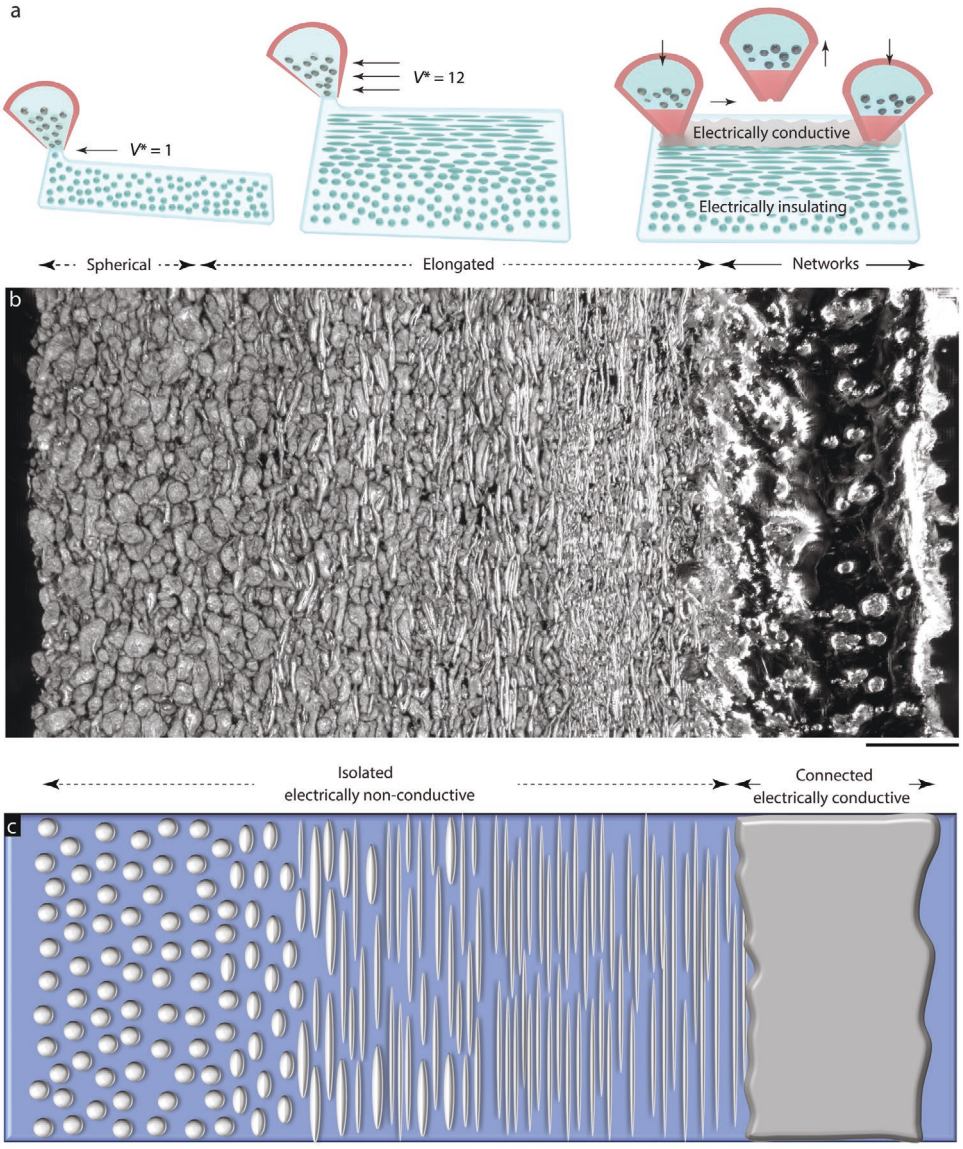

Figure 6. LM microstructure control and formation of connected networks. a) Schematics illustrating the different printing process conditions that are utilized to achieve full control of LM droplet shape, orientation, and connectivity throughout a printed part using a single printing nozzle and emulsion ink. b) Optical microscopy image of LM droplets in the printed film starting from electrically insulating (left) spherical droplets to (middle) elongated droplets to (right) connected networks that are electrically conductive. Scale bar = 500 µm. c) Schematic illustration of the shape, orientation, and connectivity of the LM droplets in the printed film.

4. Experimental Section

Materials and Fabrication of LM Ink: The LM emulsion inks were fabricated by dispersing microdroplets of eutectic gallium indium alloy (Ga:In in the ratio 3:1 by mass) in a two-component silicone elastomer (Ex-Sil 100; Gelest Inc.). First, the two-part silicone prepolymer was prepared by combining part A and part B at a 100:1 ratio by mass, then mixing and degassing in a planetary centrifugal mixer (Flaktek Speedmixer). The emulsion was formed by adding LM at 50% by volume to the silicone prepolymer and further mixing for 1 min at 2300 rpm for $D = 20$ µm and 800 rpm for $D = 100$, 200 µm. To obtain the $D = 200$ µm size, hexane was added to the elastomer in a 1:8 ratio by weight before the addition of LM. The hexane was removed before printing by placing the ink in a vacuum chamber for 2.5 h. To ensure a similar treatment before printing, the inks with $D = 20$, 100 µm were also degassed to remove trapped air voids and allowed to sit for 2.5 h after mixing. The ink was then loaded into a syringe for DIW, printed, and cured in a convection oven at 100 °C for 24 h.

Direct Ink Writing Setup: A Hyrel Engine SR 3D printer with SDS-10 head was modified to level the bed. A thin layer of Sylgard 184 (10:1 ratio) was cast on the aluminum bed and a 170 × 170 mm glass sheet was placed on the top. A thin layer of Ecoflex 00-30 was spin coated on a 70 mm-diameter glass disk, which was attached to the glass sheet on the bed. Single-layer prints are printed on a 4-mil PET film (McMaster-Carr) adhered to the Ecoflex bed for convenience of removal and handling. Optimum SmoothFlow nozzles (Nordson EFD) with 0.84 mm diameter were used to extrude the ink. An extrusion velocity of $C = 6.8$ mm s^{-1} was used for $V^* = 1$, 3, 6 filaments, and $C = 4.2$ mm s^{-1} was used for $V^* = 12$ filaments. Print head velocity was $V = 6.8$, 20.4, 40.8, and 50.4 for $V^* = 1$, 3, 6, 12 filaments, respectively.

Multilayer and Multimaterial Printing: For multilayer prints, 5-mil polycarbonate film (McMaster-Carr) was used as the substrate. Each

layer was partially cured before printing the next using a hot-air gun set to 130 °C for 5 min, followed by cooling with a fan for 6 min. The hot-air gun was attached as a print head to the H3D mounting system and controlled using an auxiliary output to provide directed heating and automate the partial curing process. The cooling fan was rigidly attached to the print bed and controlled using an auxiliary output to increase convection heat transfer. Before each layer, the syringe plunger was depressed at the desired velocity for 1 min to allow the extrusion velocity to reach equilibrium. Films containing both spherical and elongated droplets (Figure 4d,f,g) were composed of one layer of spherical droplets printed at $V^* = 2$, $H = 210$ µm and three layers of elongated droplets printed at $V^* = 12$, $H = 70$ µm, with a constant extrusion velocity of $C = 4.1$ mm s^{-1}. The fully filled right angled triangular prism contains 133 layers. The printing parameters were updated each layer using the following equations: $V^* = 1 + 11 \times ((\text{layer number} - 1)/132)$ and $H = 260 \times (V^*)^{-0.7}$ µm. For multimaterial printing, a second SDS-10 print head was added to the printer, loading one print head with Ex-Sil 100 and the other with the LM emulsion ink.

LM networks were formed with filaments that were printed as previously described using $V^* = 4$ and $H = 105$ µm. After printing, the filament was partially cured using a hot air gun set to 130 °C for 5 min. The printed filament was then electrically activated using a tapping motion with the printing nozzle. To perform the tapping motion, the nozzle was brought to a height of $H/8$, moved along the desired path by 60 µm, retracted to $2H$, and then moved along the desired path by 60 µm. This process was repeated until the desired LM network was formed.

Microscopy and Particle Analysis: Before imaging, a layer of Sylgard 184 was deposited over each sample to reduce glare from the LM droplets. Optical microscopy images were obtained using a Zeiss Axio Zoom v16 stereo microscope. Image analysis was performed using Fiji software. The LM droplets were manually outlined on the microscopy image and a mask was created with dark regions for droplets and a bright background for the matrix. Gaussian fits were performed on inclusion histograms to obtain a mean and standard deviation for the distributions. Analysis for micrographs is presented in Figure 2. A sequence of the actual microscopy image, outlines around the droplets, and the final ellipses fit on the droplets can be found in the Supporting Information (Figure S6, Supporting Information).

Mechanical Characterization: Uniaxial tension tests were performed on an Instron 5944 mechanical testing machine. Printed single- and multifilament samples were attached with tape on either end, and this section was inserted in the pneumatically controlled grips. The tested length of the filaments between the grips was ≈40 mm. Samples were strained at an extension rate of 1 mm s^{-1}. The tensile modulus was calculated from the slope of the stress–strain curve up to 5% strain.

Thermal Imaging Demonstration: Two different patterns were analyzed with elongated droplets as the letters "N" and "VT" and spherical droplets at other regions. The samples were kept on the 5-mil polycarbonate film and placed on a hot plate set to 50 °C. IR images were captured with a FLIR A655sc IR camera at a frame rate of 25 frames per second with emissivity = 0.95 and reflection temperature = 20 °C.

Thermal Management Demonstration: LM traces were spray coated using a nitrogen-assisted masking deposition technique to form interconnects on top of the composite. Then four LEDs (Cree XLamp XHP50) were placed on the surface of the composite in contact with the LM trace. The composite was placed on an aluminum block and a current of 0.5 A was applied to the 4-LED circuit in series for 40 s and then switched off. An IR camera (FLIR E54sc) was used to capture the thermal distribution.

Electrical Characterization of Printed Filaments: Electrical measurements were performed using a Fluke 117 True RMS multimeter. Stainless steel needles (25 gauge) were attached to the multimeter probes for measuring resistance of a single droplet and regions around it (Figure S7, Supporting Information).

Statistical Analysis: Data were analyzed as received from the instrument and was pre-processed and outliers were not removed. Data for multiple trials is presented as mean ± standard deviation (SD), where n is indicated in the figure legend, or presented as individual data sets.

Supporting Information

Supporting Information is available from the Wiley Online Library or from the author.

Acknowledgements

A.H. and R.T. contributed equally to this work. A.H. and E.M. acknowledge support through the NSF (No. CMMI-2054411), NASA Nebraska EPSCoR (80NSSC19M0065), and the Nebraska Tobacco Settlement Biomedical Research Development. R.T. and M.B. acknowledge support through Defense Advanced Research Projects Agency Young Faculty Award (DARPA YFA) (D18AP00041) and NSF (No. CMMI-2054409).

Conflict of Interest

The authors declare no conflict of interest.

Data Availability Statement

The data that support the findings of this study are available from the corresponding author upon reasonable request.

Keywords

3D printing, additive manufacturing, liquid metals, microstructures, soft robots

Received: January 7, 2022
Revised: March 23, 2022
Published online:

[1] R. L. Truby, J. A. Lewis, *Nature* **2016**, *540*, 371.
[2] H. Yuk, X. Zhao, *Adv. Mater.* **2018**, *30*, 1704028.
[3] T. Wallin, J. Pikul, R. Shepherd, *Nat. Rev. Mater.* **2018**, *3*, 84.
[4] S. Abdollahi, E. J. Markvicka, C. Majidi, A. W. Feinberg, *Adv. Healthcare Mater.* **2020**, *9*, 1901735.
[5] A. Lee, A. Hudson, D. Shiwarski, J. Tashman, T. Hinton, S. Yerneni, J. Bliley, P. Campbell, A. Feinberg, *Science* **2019**, *365*, 482.
[6] D. J. Braconnier, R. E. Jensen, A. M. Peterson, *Addit. Manuf.* **2020**, *31*, 100924.
[7] Y. Kim, H. Yuk, R. Zhao, S. A. Chester, X. Zhao, *Nature* **2018**, *558*, 274.
[8] S. Gantenbein, K. Masania, W. Woigk, J. P. Sesseg, T. A. Tervoort, A. R. Studart, *Nature* **2018**, *561*, 226.
[9] Q. Ge, H. J. Qi, M. L. Dunn, *Appl. Phys. Lett.* **2013**, *103*, 131901.
[10] A. S. Gladman, E. A. Matsumoto, R. G. Nuzzo, L. Mahadevan, J. A. Lewis, *Nat. Mater.* **2016**, *15*, 413.
[11] M. Wehner, R. L. Truby, D. J. Fitzgerald, B. Mosadegh, G. M. Whitesides, J. A. Lewis, R. J. Wood, *Nature* **2016**, *536*, 451.
[12] D. K. Patel, A. H. Sakhaei, M. Layani, B. Zhang, Q. Ge, S. Magdassi, *Adv. Mater.* **2017**, *29*, 1606000.
[13] M. A. Skylar-Scott, J. Mueller, C. W. Visser, J. A. Lewis, *Nature* **2019**, *575*, 330.

[14] A. D. Valentine, T. A. Busbee, J. W. Boley, J. R. Raney, A. Chortos, A. Kotikian, J. D. Berrigan, M. F. Durstock, J. A. Lewis, *Adv. Mater.* **2017**, *29*, 1703817.
[15] J. Odent, T. J. Wallin, W. Pan, K. Kruemplestaedter, R. F. Shepherd, E. P. Giannelis, *Adv. Funct. Mater.* **2017**, *27*, 1701807.
[16] J. T. Muth, D. M. Vogt, R. L. Truby, Y. Mengüç, D. B. Kolesky, R. J. Wood, J. A. Lewis, *Adv. Mater.* **2014**, *26*, 6307.
[17] M. G. Mohammed, R. Kramer, *Adv. Mater.* **2017**, *29*, 1604965.
[18] I. D. Joshipura, H. R. Ayers, C. Majidi, M. D. Dickey, *J. Materi. Chem. C* **2015**, *3*, 3834.
[19] S.-Z. Guo, K. Qiu, F. Meng, S. H. Park, M. C. McAlpine, *Adv. Mater.* **2017**, *29*, 1701218.
[20] J. W. Boley, E. L. White, G. T.-C. Chiu, R. K. Kramer, *Adv. Funct. Mater.* **2014**, *24*, 3501.
[21] M. D. Dickey, R. C. Chiechi, R. J. Larsen, E. A. Weiss, D. A. Weitz, G. M. Whitesides, *Adv. Funct. Mater.* **2008**, *18*, 1097.
[22] T. Liu, P. Sen, C.-J. Kim, *J. Microelectromech. Syst.* **2011**, *21*, 443.
[23] M. A. Creighton, M. C. Yuen, M. A. Susner, Z. Farrell, B. Maruyama, C. E. Tabor, *Langmuir* **2020**, *36*, 12933.
[24] M. D. Dickey, *Adv. Mater.* **2017**, *29*, 1606425.
[25] Z. Ma, Q. Huang, Q. Xu, Q. Zhuang, X. Zhao, Y. Yang, H. Qiu, Z. Yang, C. Wang, Y. Chai, Z. Zheng, *Nat. Mater.* **2021**, *20*, 859.
[26] N. Kazem, M. D. Bartlett, C. Majidi, *Adv. Mater.* **2018**, *30*, 1706594.
[27] R. Tutika, S. H. Zhou, R. E. Napolitano, M. D. Bartlett, *Adv. Funct. Mater.* **2018**, *28*, 1804336.
[28] M. I. Ralphs, N. Kemme, P. B. Vartak, E. Joseph, S. Tipnis, S. Turnage, K. N. Solanki, R. Y. Wang, K. Rykaczewski, *ACS Appl. Mater. Interfaces* **2018**, *10*, 2083.
[29] M. H. Malakooti, N. Kazem, J. Yan, C. Pan, E. J. Markvicka, K. Matyjaszewski, C. Majidi, *Adv. Funct. Materi.* **2019**, *29*, 1906098.
[30] R. Tutika, S. Kmiec, A. T. Haque, S. W. Martin, M. D. Bartlett, *ACS Appl. Mater. Interfaces* **2019**, *11*, 17873.
[31] J. Wang, G. Cai, S. Li, D. Gao, J. Xiong, P. S. Lee, *Adv. Mater.* **2018**, *30*, 1706157.
[32] A. Kataruka, S. B. Hutchens, *Soft Matter* **2019**, *15*, 9665.
[33] E. J. Krings, H. Zhang, S. Sarin, J. E. Shield, S. Ryu, E. J. Markvicka, *Small* **2021**, *17*, 2104762.
[34] S. Mei, Y. Gao, Z. Deng, J. Liu, *J. Electron. Packag.* **2014**, *136*, 011009.
[35] M. J. Ford, C. P. Ambulo, T. A. Kent, E. J. Markvicka, C. Pan, J. Malen, T. H. Ware, C. Majidi, *Proc. Natl. Acad. Sci. USA* **2019**, *116*, 21438.
[36] C. Pan, E. J. Markvicka, M. H. Malakooti, J. Yan, L. Hu, K. Matyjaszewski, C. Majidi, *Adv. Mater.* **2019**, *31*, 1900663.
[37] P. Testa, R. W. Style, J. Cui, C. Donnelly, E. Borisova, P. M. Derlet, E. R. Dufresne, L. J. Heyderman, *Adv. Mater.* **2019**, *31*, 1900561.
[38] B. S. Chang, R. Tutika, J. Cutinho, S. Oyola-Reynoso, J. Chen, M. D. Bartlett, M. M. Thuo, *Mater. Horiz.* **2018**, *5*, 416.
[39] T. L. Buckner, M. C. Yuen, S. Y. Kim, R. Kramer-Bottiglio, *Adv. Funct. Mater.* **2019**, *29*, 1903368.
[40] E. J. Markvicka, M. D. Bartlett, X. Huang, C. Majidi, *Nat. Mater.* **2018**, *17*, 618.
[41] E. J. Markvicka, R. Tutika, M. D. Bartlett, C. Majidi, *Adv. Funct. Mater.* **2019**, *29*, 1900160.
[42] J. W. Boley, E. L. White, R. K. Kramer, *Adv. Mater.* **2015**, *27*, 2355.
[43] Y. Lin, C. Cooper, M. Wang, J. J. Adams, J. Genzer, M. D. Dickey, *Small* **2015**, *11*, 6397.
[44] C. J. Thrasher, Z. J. Farrell, N. J. Morris, C. L. Willey, C. E. Tabor, *Adv. Mater.* **2019**, *31*, 1903864.
[45] S. Liu, M. C. Yuen, E. L. White, J. W. Boley, B. Deng, G. J. Cheng, R. Kramer-Bottiglio, *ACS Appl. Mater. Interfaces* **2018**, *10*, 28232.
[46] M. D. Bartlett, N. Kazem, M. J. Powell-Palm, X. Huang, W. Sun, J. A. Malen, C. Majidi, *Proc. Natl Acad Sci. USA* **2017**, *114*, 2143.
[47] M. D. Bartlett, M. D. Dickey, C. Majidi, *NPG Asia Mater.* **2019**, *11*, 21.
[48] R. Tutika, A. T. Haque, M. D. Bartlett, *Commun. Mater.* **2021**, *2*, 64.
[49] S. Liu, D. S. Shah, R. Kramer-Bottiglio, *Nat. Mater.* **2021**, *20*, 851.
[50] A. Fassler, C. Majidi, *Adv. Mater.* **2015**, *27*, 1928.
[51] A. T. Haque, R. Tutika, R. L. Byrum, M. D. Bartlett, *Adv. Funct. Mater.* **2020**, *30*, 2000832.
[52] R. W. Style, R. Tutika, J. Y. Kim, M. D. Bartlett, *Adv. Funct. Mater.* **2021**, *31*, 2005804.
[53] S. Chen, H.-Z. Wang, R.-Q. Zhao, W. Rao, J. Liu, *Matter* **2020**, *2*, 1446.
[54] C. Ma, S. Wu, Q. Ze, X. Kuang, R. Zhang, H. J. Qi, R. Zhao, *ACS Appl. Mater. Interfaces* **2020**, *13*, 12639.
[55] A. Kotikian, R. L. Truby, J. W. Boley, T. J. White, J. A. Lewis, *Adv. Mater.* **2018**, *30*, 1706164.
[56] D. J. Roach, X. Kuang, C. Yuan, K. Chen, H. J. Qi, *Smart Mater. Struct.* **2018**, *27*, 125011.
[57] B. G. Compton, J. A. Lewis, *Adv. Mater.* **2014**, *26*, 5930.
[58] G. Franchin, H. S. Maden, L. Wahl, A. Baliello, M. Pasetto, P. Colombo, *Materials* **2018**, *11*, 515.
[59] H. L. Tekinalp, V. Kunc, G. M. Velez-Garcia, C. E. Duty, L. J. Love, A. K. Naskar, C. A. Blue, S. Ozcan, *Compos. Sci. Technol.* **2014**, *105*, 144.
[60] L.-y. Zhou, J.-z. Fu, Q. Gao, P. Zhao, Y. He, *Adv. Funct. Mater.* **2019**, *30*, 1906683.
[61] T. V. Neumann, E. G. Facchine, B. Leonardo, S. Khan, M. D. Dickey, *Soft Matter* **2020**, *16*, 6608.
[62] R. Tandel, B. A. Gozen, *J. Mater. Process. Technol.* **2021**, *302*, 117470.
[63] L.-y. Zhou, J.-h. Ye, J.-z. Fu, Q. Gao, Y. He, *ACS Appl. Mater. Interfaces* **2020**, *12*, 12068.
[64] Y. Zheng, Z. He, Y. Gao, J. Liu, *Sci. Rep.* **2013**, *3*, 1786.
[65] H. Chang, R. Guo, Z. Sun, H. Wang, Y. Hou, Q. Wang, W. Rao, J. Liu, *Adv. Mater. Interfaces* **2018**, *5*, 1800571.
[66] F. Deng, Q.-K. Nguyen, P. Zhang, *Addit. Manuf.* **2020**, *33*, 101117.
[67] W. Zhang, J. Chen, X. Li, Y. Lu, *Small* **2020**, *16*, 2004190.
[68] X. Wang, L. Li, X. Yang, H. Wang, J. Guo, Y. Wang, X. Chen, L. Hu, *Adv. Mater. Technol.* **2021**, *6*, 2100228.
[69] Y. Yu, F. Liu, R. Zhang, J. Liu, *Adv. Mater. Technol.* **2017**, *2*, 1700173.
[70] J.-Y. Gao, S. Chen, T.-Y. Liu, J. Ye, J. Liu, *Mater. Today* **2021**, *49*, 201.
[71] T. V. Neumann, M. D. Dickey, *Adv. Mater. Technol.* **2020**, *5*, 2000070.
[72] M. Rajagopalan, M. Bhatia, M. Tschopp, D. Srolovitz, K. Solanki, *Acta Mater.* **2014**, *73*, 312.